Iraqi Journal of Physics, 2026
https://doi.org/10.30723/ijp.v24i3.1449

Vol.24, No.3, PP.25-38
P-ISSN: 2070-4003
E-ISSN: 2664-5548

The Influence of Dopants on the Structural and Optical Properties of SnO_2 Thin Films Deposited by PLD for Gas Sensor Application

Ismail S. Najm[1*] and Iqbal S. Naji[1]
[1]*Department of Physics, College of Science, University of Baghdad, Baghdad, Iraq*
[*]Corresponding author: Ismail.najm2304@sc.uobaghdad.edu.iq

Abstract

This study investigated the effects of different dopants (Mn, Cu, and Sb) on the characterization of SnO_2 thin films prepared by pulsed laser deposition (PLD). The pure and doped powders were prepared by the sol-gel technique and sintered at 600 ^oC for two hours. Structural analysis revealed a tetragonal structure in SnO_2, and the addition of dopants induced lattice strain and increased dislocation density, thereby enhancing the number of active sites available for gas interactions. The morphology analysis revealed that the particles were uniformly distributed in the films and were almost spherical in shape. Optical measurements demonstrated a bandgap change, which decreased with doping from 3.83 to 2.86 eV. The higher sensitivity toward 50 ppm NO_2 at 100°C operating temperature was 41.6% for the film doped with Sb compared with films doped with Mn and Cu (25% and 24%). The results showed the different impacts of different dopants in enhancing the structural and optical properties of SnO_2 thin films, which affect the sensor sensitivity toward NO_2 gas.

Article Info.

Keywords:
Tin Oxide, Thin Film, PLD Method, Doped SnO_2, Gas Sensor.

Article history:
Received:Mar. 15, 2025
Revised: Jul. 03, 2025
Accepted: Jul. 25, 2025
Published:Sep.01,2026

1. Introduction

Transparent Conducting Oxides (TCOs) are a new class of materials that have two paradoxical properties simultaneously, which are optical transparency and conductivity [1]. Compared to other metal oxides, tin dioxide (SnO_2) is a transparent conducting oxide; it is an n-type semiconductor with a wide direct band gap of 3.6 eV and a high exciton binding energy of 130 meV. It has several advantages, including its availability, ease of fabrication, low cost, and excellent optical and electrical properties, which are related to its chemical and physical stabilities in harsh environments [2-5].

These properties make it an attractive material for several applications, such as solar cells, planar waveguides, antireflective coatings, electronic sensors, liquid crystal displays, and optical filters. SnO_2 is not limited to the research laboratory, but is used commercially in environmental monitoring, health care, and industrial safety applications [6-7]. Thin films of SnO_2 are widely utilized in gas-sensing technology, which exhibit remarkable sensitivity to a wide range of gases [8, 9]. However, undoped SnO_2 has a low electron concentration, which gives many limitations, such as poor selectivity and limited response under certain operating conditions, and can be improved through doping [6] or achieved by forming heterostructures [9]. There are many methods used to deposit SnO_2 thin films, such as the sol-gel method [10], spray pyrolysis [11], reactive magnetron sputtering [12], chemical vapour deposition [13], spin coating [14], and the pulsed laser deposition (PLD) method, which is a versatile and precise thin-film fabrication method. Also, PLD offers advantages such as relatively high deposition rate, stoichiometric transfer of the target material, and fabricating films with well-controlled structural and compositional properties at low cost [15-17].

A key technique for modifying the structural, optical, and electrical properties of SnO_2 thin films is doping, which changes the film's band gap, surface morphology, carrier concentration, and critical gas-sensing factors [18]. Additionally, dopants create active sites and defects on the surface of the SnO_2 film, enhancing the adsorption and reaction processes with gas molecules. These defects, such as oxygen vacancies and interstitial sites, act as

catalytic centers that increase the material's sensitivity to specific gases. Therefore, tailoring the dopant type is essential for achieving optimal sensing performance toward a target gas [19, 20].

In this study, we investigate the influence of different dopants on the structural, morphological, and optical properties of SnO_2 thin films deposited by the PLD method. A suitable dopant, achieved through a simple technique, was used to vary SnO_2 properties and enhance gas-sensing behavior. The findings of this work contribute to the understanding of material design for gas sensors to optimize SnO_2-based gas sensors for NO_2 gas.

2. Experimental Part

SnO_2 nanoparticle powders were prepared using the sol-gel method. First of all, 3.506 g of tin tetrachloride pentahydrate ($SnCl_4.5H_2O$, 98%) (Supplied from Loba Chemie Pvt. Ltd., India), as a source of Sn^{+4} ions, was dissolved in a mixture of 45 mL deionized water and 5 mL ethylene glycol. The solution was stirred on a magnetic stirrer at 60 °C. After 2 hrs, 0.5 M aqueous ammonia solution (from Thomas Baker (Chemicals) Pvt. Ltd.) was dropwise added to the above solution with stirring. The resulting gel was dried at 80 ºC for 48 hrs to remove water molecules. Finally, white colored tin oxide nanopowders were formed at 600ºC for 2 hrs. The same procedure was followed for the preparation of SnO_2 doped with 10 wt.% (Sb, Cu, Mn) using antimony trichloride ($SbCl_3$ 98.5%) (Supplied from HiMedia Laboratories), cupric chloride dehydrate ($CuCl_2.2H_2O$ 98%) (Supplied from Loba Chemie Pvt Ltd.), and Manganese chloride ($MnCl_2$ $4H_2O$ 99%) (Supplied from Pub.Chem), respectively.

The produced powder samples were converted into pellets under a pressure of 10 Tons to be used as targets of 2 cm in diameter and 0.5 cm in thickness. After the targets' preparation, the sintering process was done at 600 °C for 1 hr. Pure and doped SnO2 thin films were deposited on glass slides using the PLD technique with a Q-switched Nd: YAG laser (Diamond-288) of 1064 nm wavelength, 10 ns pulse duration, and 6 Hz repetition frequency. Film deposition was conducted in a vacuum glass chamber at 10^{-2} mbar. The ablation target was fixed vertically and aligned with the substrate at a 2 cm target-to-substrate distance. A Q-switched Nd: YAG laser beam was focused onto the target at an incidence angle of 45°. The laser source was located such that the target was at the focal point of the laser lens. The deposition process was done using 200 pulses and an energy of 800 mJ. The prepared thin films were annealed at 200°C for 30 minutes to enhance the samples' crystallinity.

3. Characterization Technique

The structural properties, surface morphology, optical and electrical properties of the deposited thin film were investigated by XRD (using a 6000-Shimadzu, Japan diffractometer), scanning electron microscopy (MIRA TESCAN), UV-visible (Metertech SP-8001) spectrophotometer, within the 100–1100 nm wavelength range, and Van der Pauw Ecopia HMS-3000 Hall measurement system.

Gas sensor devices were arranged by depositing mesh aluminum electrodes onto the sample surfaces using the thermal evaporation Edward system, and then connecting them with thin wires using silver paste. Gas sensing was examined at a controlled temperature in a closed chamber. The sample was electrically connected to an electronic circuit connected to a computer. The NO_2-Air were mixed using two flow meters in the chamber at specific ratios.

4. Results and Discussions

The X-ray diffraction (XRD) patterns of pure and doped thin films with the three dopants Mn, Cu, and Sb prepared by the PLD technique from the synthesized targets are shown in Fig. 1. All samples appeared as polycrystalline structures. The peaks located at diffraction angles of 26.57°, 33.81°, and 51.68° matched the crystallite lattice planes (110), (101), and

(211) of the tetragonal structure of SnO_2 according to JCPDS Card No. 96-900-9083. Small shifts appeared in the diffraction peaks for all doped samples due to induced strain within the lattice by substituting with different dopants of different ionic radii than the tin cation. No additional phase was observed in the doped samples, indicating that the incorporation of these unusual ions into the SnO_2 lattice in a limited amount does not alter the entire lattice and instead fully incorporates these additions without forming a separate phase. The broadening of the diffraction lines indicates the nanocrystalline form.

The crystallite size (D) was calculated utilizing the Debye–Scherrer's formula as shown in Table 1:

$$D = \frac{k\lambda}{\beta \cos\theta} \quad (1)$$

where k is the shape factor (0.94), λ is equal to 1.54060 Å, β is the full width at half maximum (FWHM), and θ is the diffraction angle. The mean crystallite sizes were 15.8, 15.3, 17.7, and 17.8 nm for the pure SnO_2 and the Mn, Cu, and Sb-doped samples, respectively.

The larger crystallites cause less lattice strain, which can contribute to more defined crystalline growth and lower defect density in the films. More crystallinity causes a significant impact on the optical and electrical properties of the thin films, mainly when applied to gas sensors, photocatalysts, or other functional devices.

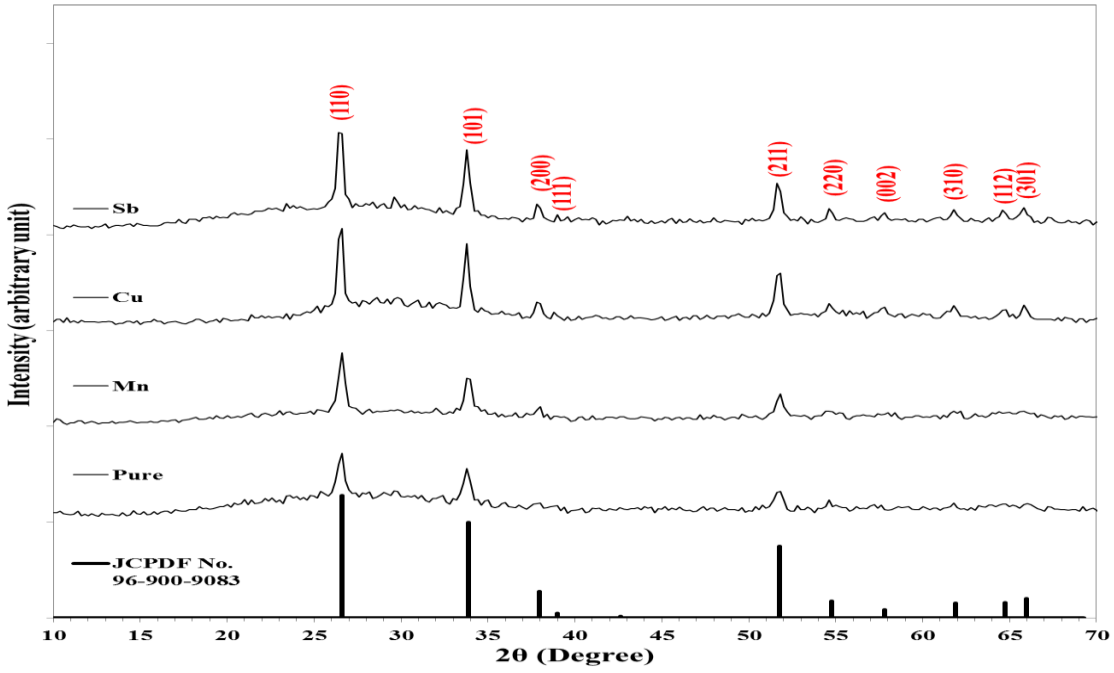

Figure 1: XRD patterns of the pure and doped SnO_2 thin films with the three dopants deposited by the PLD method.

The lattice parameters for the tetragonal structure (a and c) for the pure and doped SnO_2 were determined using the diffraction lines (110) and (101) utilizing the relation [21]:

$$\frac{1}{d_{hkl}^2} = \frac{h^2 + k^2}{a^2} + \frac{l^2}{b^2} \quad (2)$$

Table 1 lists the (d_{hkl}), microstrain (ε), and dislocation density (δ) for each crystalline direction of the prepared samples.

Table 1: XRD parameters of the pure and doped SnO_2 thin films with the three dopants Mn, Cu, and Sb.

Sample	2θ (°)	FWHM (°)	d_{hkl} (Å)	D (nm)	ε ×10^{-2}	δ (nm^{-2})	hkl
Pure SnO_2	26.5688	0.5400	3.3523	15.8	1.00	0.0040	(110)
	33.8133	0.5800	2.6488	15.0	0.83	0.0044	(101)
	51.6821	0.6700	1.7672	13.8	0.60	0.0052	(211)
SnO_2:Mn	26.6068	0.5573	3.3476	15.3	1.03	0.0042	(110)
	33.8885	0.5202	2.6431	16.7	0.75	0.0035	(101)
	51.7585	0.5201	1.7648	17.7	0.47	0.0032	(211)
SnO_2:Cu	26.5697	0.4830	3.3522	17.7	0.89	0.0032	(110)
	33.8142	0.4458	2.6487	19.5	0.64	0.0026	(101)
	51.7214	0.5202	1.7660	17.7	0.47	0.0032	(211)
SnO_2:Sb	26.4582	0.4829	3.3660	17.8	0.90	0.0032	(110)
	33.8142	0.4459	2.6487	19.5	0.64	0.0026	(101)
	51.6099	0.4459	1.7695	20.7	0.40	0.0023	(211)

The lattice constant values of the pure SnO_2 and the three dopants are listed in Table 2 and are very close to the standard value. There are slight variations in lattice constants after doping with the three dopants.

Table 2: The variation of lattice constants of the pure and doped-SnO_2 thin films, prepared by PLD with the three dopants Mn, Cu, and Sb.

Sample	a (Å)	c (Å)
Pure SnO_2	4.7407	3.1937
Mn-doped	4.7342	3.1858
Cu-doped	4.7406	3.1937
Sb-doped	4.7603	3.1878

Field Emission Scanning Electron Microscope (FESEM) analysis gives information about the surface topography and uniformity of the samples. Fig. 2 displays the FESEM images of undoped and doped tin oxide thin films with two magnifications (60000x and 120000x). All samples revealed that the particles were uniformly distributed in the films and were almost spherical in shape. The average particle diameter was 39, 45, 72, and 40 nm for pure and Mn, Cu, and Sb-doped SnO_2 films, respectively.

To estimate the thickness of SnO_2 thin films prepared by PLD, cross-section analysis was used. Fig. 3 shows the cross-sectional FESEM images with two magnifications of 8 and 30 kx. The sample appeared to have an average cross-sectional thickness of 1300 nm.

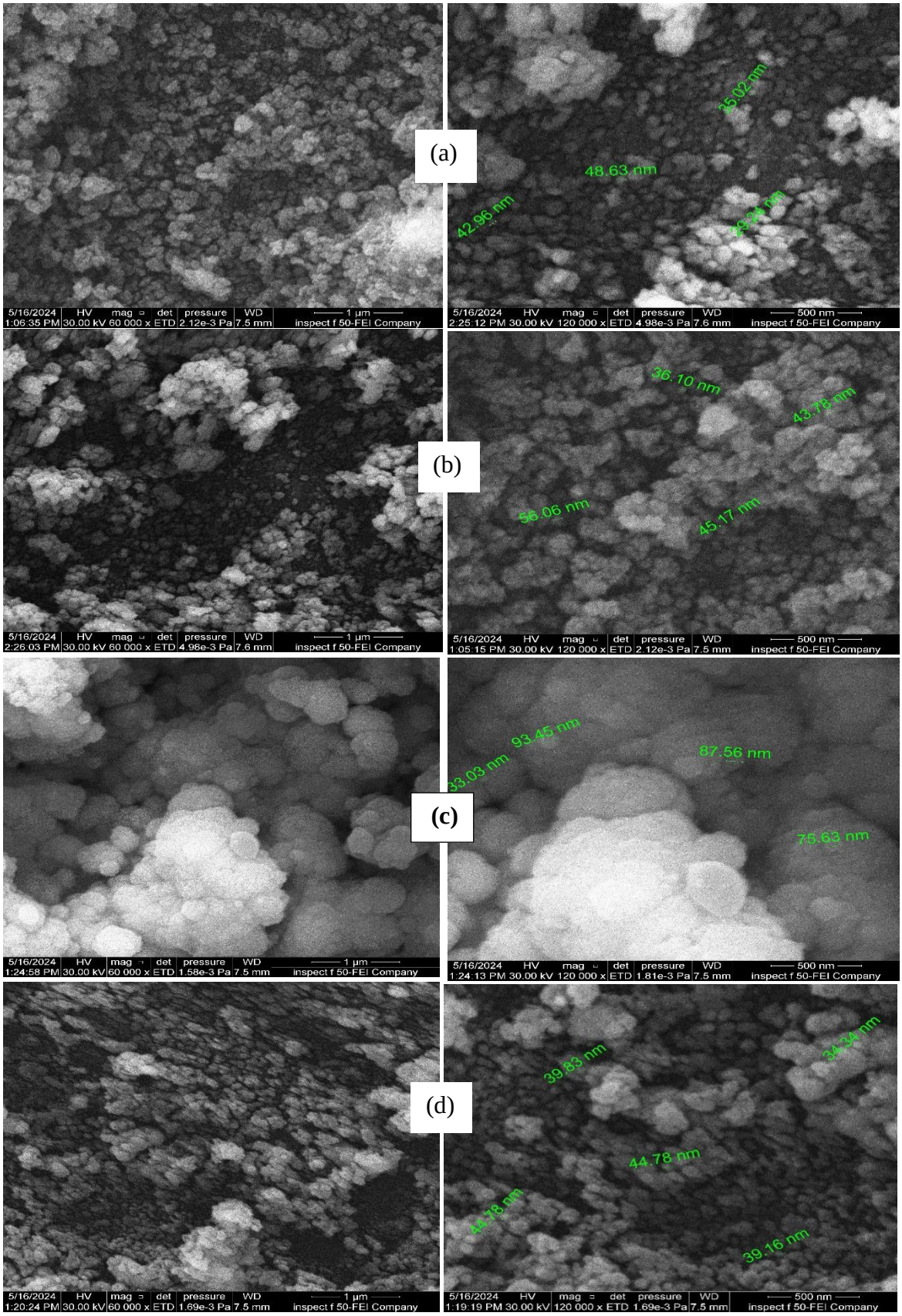

Figure 2: Top-view FESEM images at two magnifications of (a) pure SnO_2, (b) Cu-doped, (c) Mn-doped, and (d) Sb-doped thin films.

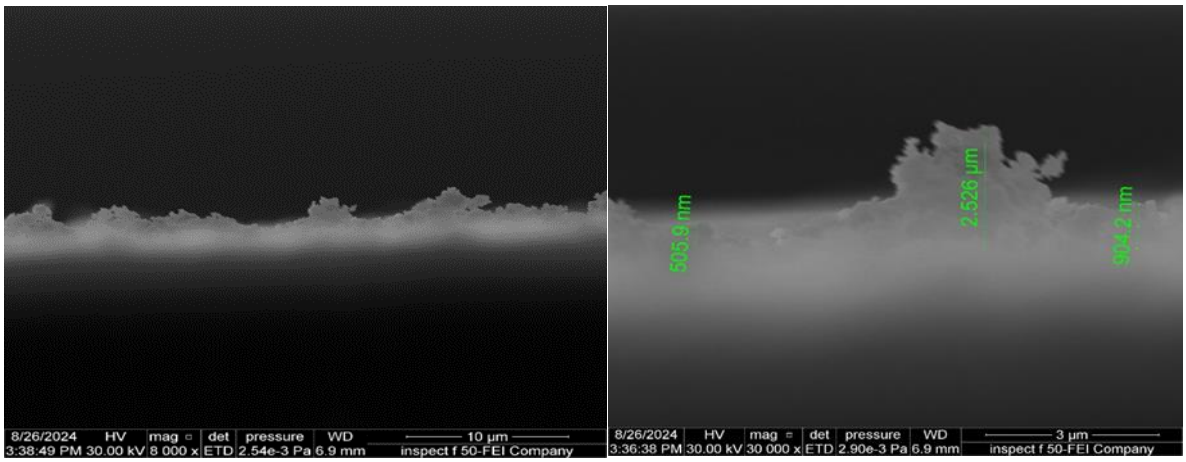

Figure 3: Cross-section FESEM images of SnO_2 thin films prepared by PLD.

Fig. 4 shows the absorption coefficient spectra of the undoped SnO_2 and the doped thin films deposited on glass substrates as a function of the wavelength within the range of 300 to 1100 nm. The absorption coefficient of all films decreased with increasing wavelength, and the maximum values were in the UV region. There was a red shift in the absorption peak for the doped tin oxide thin films. Undoped tin oxide thin films exhibited the lowest absorption coefficient in the visible range, indicating the highest transparency. In contrast, all the doped tin oxide thin films had lower transparency than the undoped tin oxide thin films. Because the dopant incorporation into the tin oxide lattice decreases the transparency of the tin oxide thin films. The 10 wt.% copper-doped tin oxide thin films showed the lowest transparency in all wavelength regions.

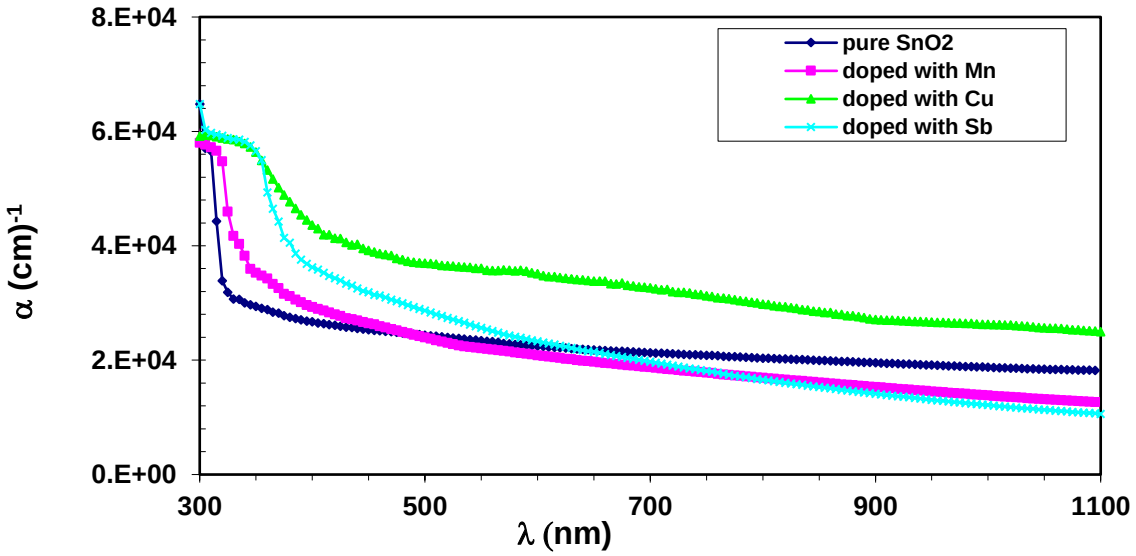

Figure 4: The relation between the absorption coefficient and wavelength of pure and doped SnO_2 thin films with three types of dopants.

The optical band gap energy (E_g) of the undoped and doped SnO_2 films was determined using the Tauc plot [22], using the relation:

$$(\alpha hv) = A\,(hv - E_g)^n \qquad (3)$$

where α is the absorption coefficient, h is the Planck constant, ν is the transition frequency, A is a constant, E_g is the band gap corresponding to a particular transition occurring in the film, and n indicates the transition type; n = 1/2 for direct allowed, n = 2 for indirect allowed, n = 3/2 for direct forbidden and n = 3 for indirect forbidden transitions. The fundamental absorption, corresponding to electron excitation from the valence band to the conduction band, can be used to determine the optical band gap energy.

Fig. 5 shows the Tauc plots for direct optical band gap energy values for undoped SnO_2 and Mn, Cu, and Sb-doped SnO_2 films, which are equal to 3.83, 3.62, 2.86, and 3.185 eV, respectively. The resulting value of the undoped SnO_2 film agrees with that of Roguai [23] and Karmaoui [24]. It is clear that the band gap energy decreased with doping; this is due to the introduction of impurity energy levels within the gap, effectively narrowing the energy difference between the valence and conduction bands.

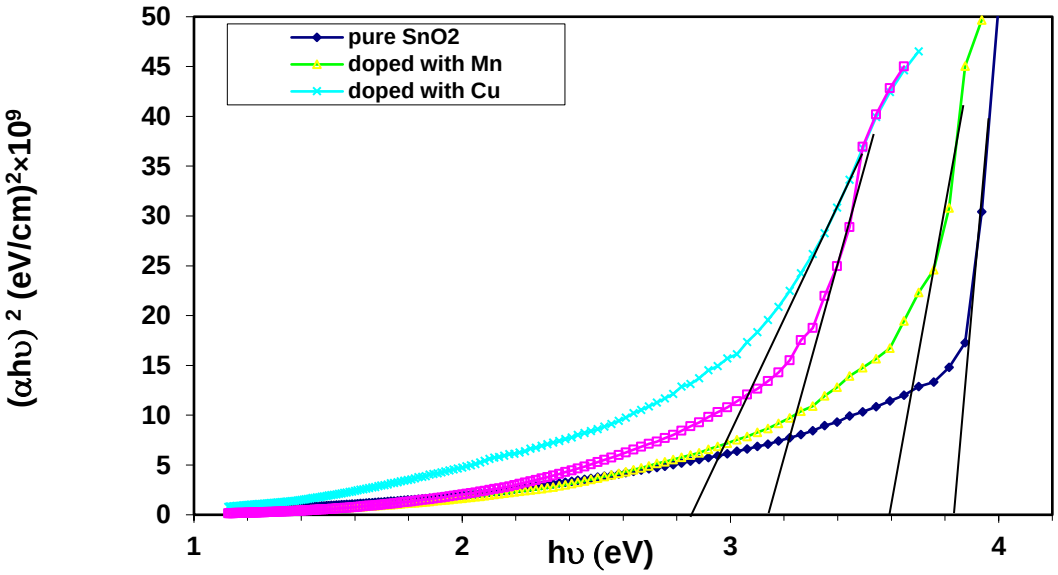

Figure 5: Tauc plots of pure and doped SnO_2 thin films using the different dopants.

Hall effect measurements were done for undoped and doped SnO_2 films with Mn, Cu, and Sb dopants. The benefits of this measurement are optimizing the behavior of a material's conductivity to determine the sensor responsivity, the semiconductor type orders, and the resistance variation (up or down) upon gas interaction. Undoped SnO_2 and doped with Mn, Cu, and Sb films show n-type conductivity. The n-type conductivity of undoped SnO_2 films was attributed to the formation of shallow donor levels occurring due to the presence of oxygen vacancies and interstitial tin in the SnO_2 lattice [25]. In the n-type SnO_2 films, the Mn^{+2}, Cu^{+2} ions replaced some of the Sn^{4+} ions, resulting in a net decrease in charge carrier concentration [26]. Manganese and Copper have two electrons less than Sn and were compensated by the conduction band electrons from the SnO_2 lattice. Antimony-doped tin oxide thin films also showed a decrease in charge carrier concentration because Sb has five electrons and these ions replace some of the Sn^{4+} ions; there was a net decrease in charge carrier concentration, but less than the Mn and Cu dopants. Resistivity, conductivity, charge carrier concentration, and mobility were obtained from the Hall measurement data. Table 3 lists the electrical parameters, including the charge carrier concentration, mobility, conductivity, and carrier type. The highest charge carrier concentration and lowest charge carrier mobility were 1.635×10^{14} cm^{-3} and 0.759 cm^2/v.s for the undoped sample.

Table 3: Hall Effect parameters of the pure and doped samples with the three dopant types.

Sample	$n_H \times 10^{13}$ (cm^{-3})	μ_H (cm^2/ v.sec)	$\sigma_{RT} \times 10^{-5}$ (Ω^{-1}. cm^{-1})	Conductivity Type
SnO_2	16.35	0.759	1.989	n-type
Mn-doped	0.679	17.79	1.935	n-type
Cu- doped	1.697	7.883	2.143	n-type
Sb- doped	7.735	1.676	2.077	n-type

Figs. 6-9 show the resistance variation with time of the fabricated sensors based on pure and doped-SnO_2 thin films prepared by the PLD method when exposed to 50 ppm NO_2 at different operating temperatures (RT, 100, and 200 °C). All samples demonstrated n-type behavior as the resistance increased with the presence of NO_2 gas molecules. The extracted electrons from the sample surface by the oxidized gas that are adsorbed on the surface increase the resistance due to variation in electron concentration as well as reduction.

The sensitivity of the sensor to gas was determined using the following equation [27]:

$$S = \left| \frac{R_g - R_a}{R_a} \right| \times 100\% \qquad (4)$$

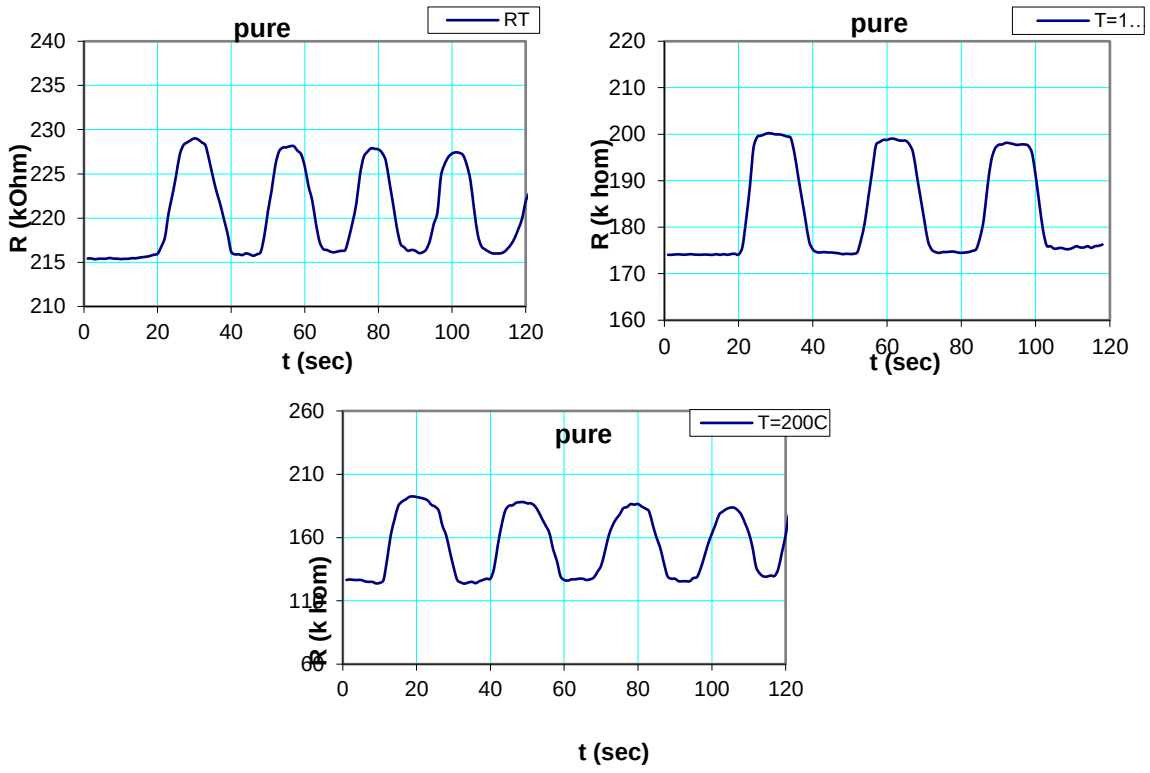

Figure 6: Resistance variation of SnO_2 thin films with 50 ppm NO_2 at different working temperatures.

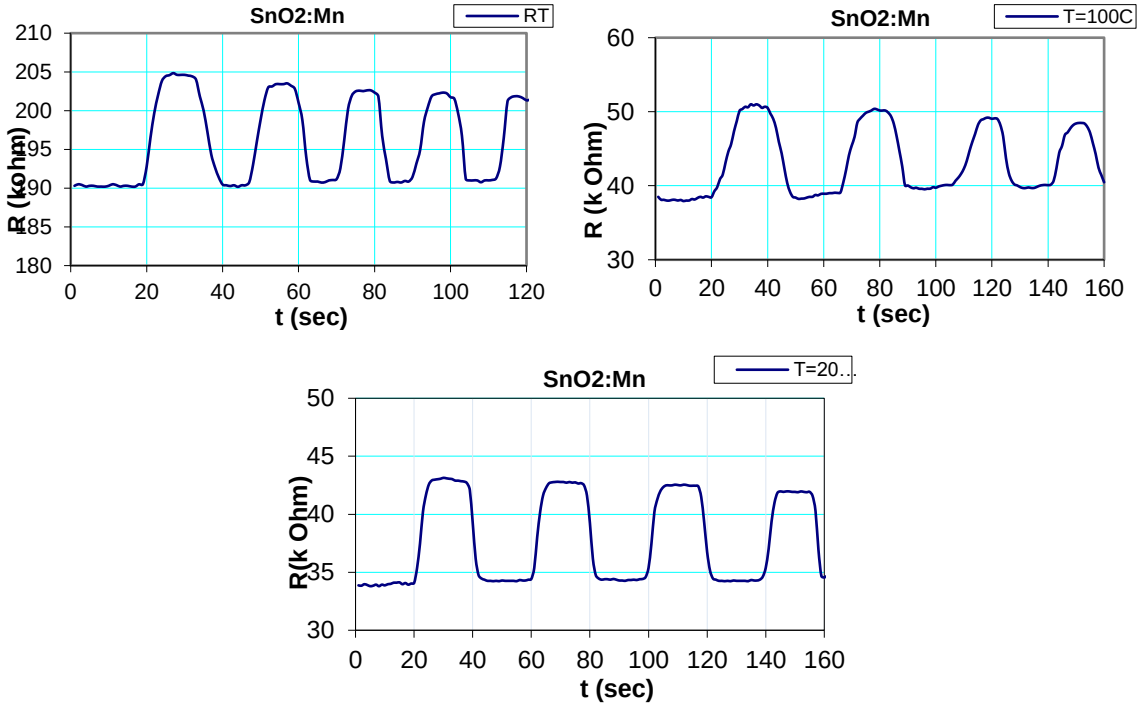

Figure 7: Resistance variation of Mn-doped SnO_2 thin films with 50 ppm NO_2 at different working temperatures.

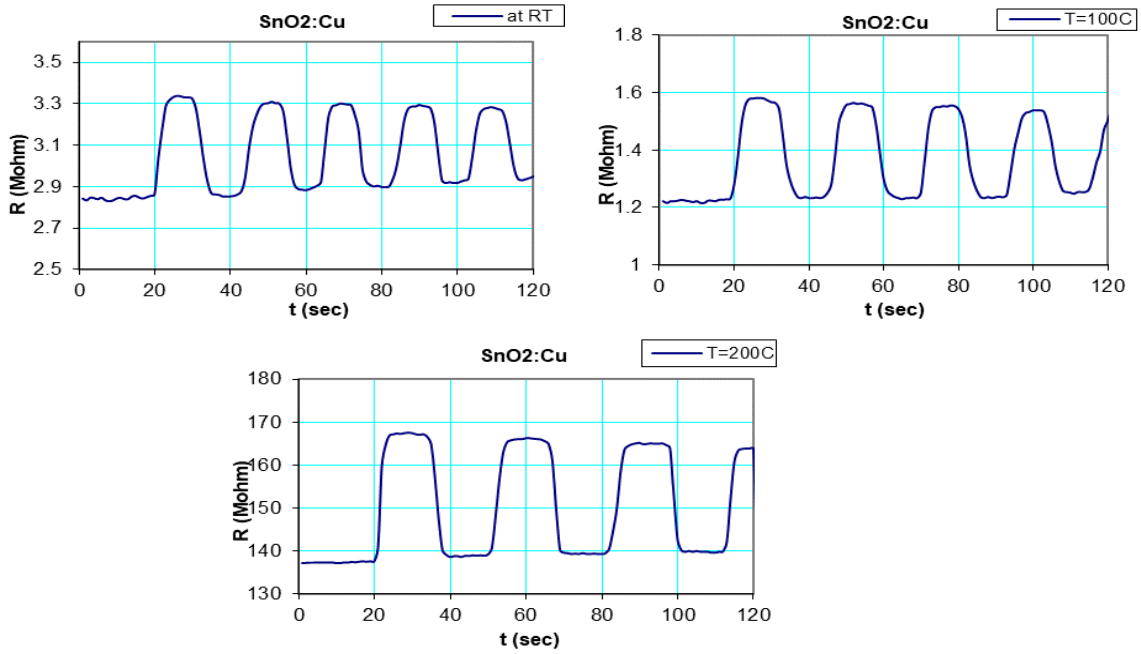

Figure 8: Resistance variation of Cu-doped SnO_2 thin films with 50 ppm NO_2 at different working temperatures.

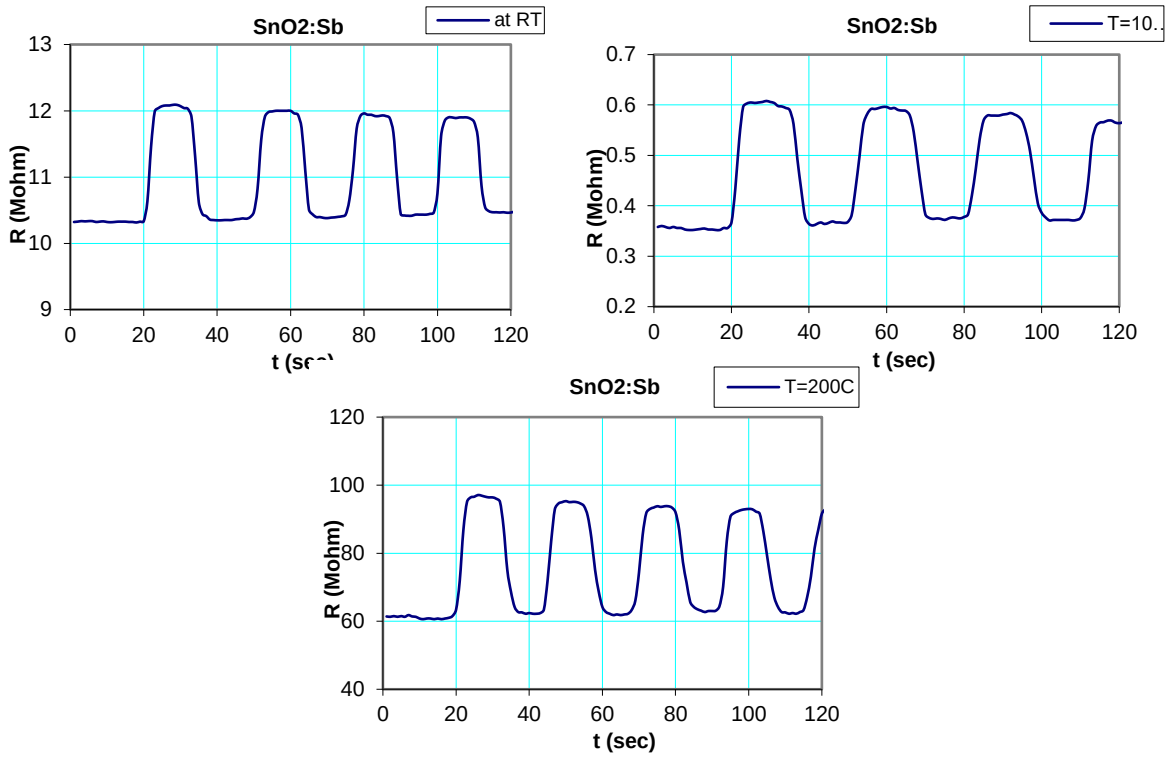

Figure 9: resistance variation of Sb-doped SnO_2 thin films with 50 ppm NO_2 at different working temperatures.

Fig. 10 demonstrates the variation in gas sensitivity to NO_2 at different operating temperatures for the pure and doped SnO_2 thin films deposited by PLD. The highest sensitivity (41.66%) was observed for the Sb-doped SnO_2 sample at an operating temperature of 100 °C. Table 4 summarizes the sensitivity, response time, and recovery time of the pure and doped SnO_2 sensors exposed to 50 ppm NO_2 gas at different operating temperatures. The response and recovery times varied depending on the dopant type and operating temperature.

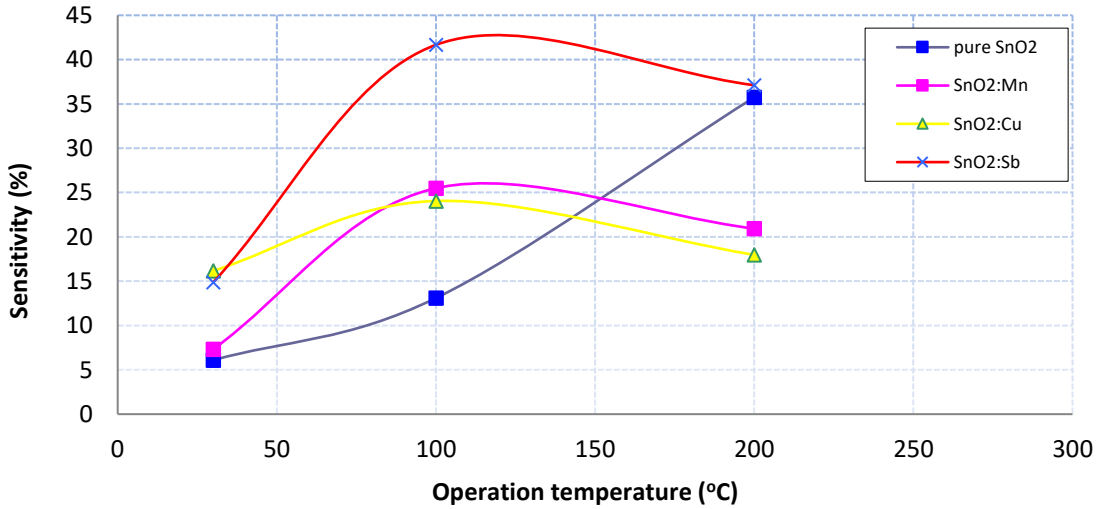

Figure 10: Gas sensor sensitivity against working temperatures based on pure and doped SnO_2 thin films using the three dopants.

Among the investigated sensors, the Sb-doped SnO_2 sensor exhibited the highest sensitivity of 41.66% toward 50 ppm NO_2 at an operating temperature of 100 °C. The sensor sensitivity highly depends on the operating temperature due to the variation in the dominant oxygen species contributing to the gas sensitivity. The sensitivity is limited at low temperatures by the $O_2^-{}_{ads}$ ion [28]. These ions dissociate into $O^-{}_{ads}$ ions with increasing temperature, causing the extraction of additional electrons and enhancing the sensor sensitivity [29]. Higher working temperatures cause a reduction in the adsorbed gases on the sample surface, retarding its sensitivity. Table 4 illustrates all parameters of undoped and doped SnO_2 gas sensors.

Doping with Mn, Cu, and Sb modifies the surface chemistry of SnO_2, altering its ability to adsorb and react with NO_2. Mn-doped samples may introduce more oxygen vacancies, enhancing NO_2 adsorption and increasing sensitivity. The Mn dopants can create oxygen vacancies in the SnO_2 lattice, which act as active sites for gas adsorption. These vacancies enhance the adsorption of NO_2. Cu can also act as a catalyst, enhancing the reactivity of the surface with NO_2. This increased interaction typically leads to a higher sensitivity.

Table 4: NO_2 gas sensor sensitivity, response time, and recovery time for sensors based on pure and doped SnO_2 thin films using the three dopants at different working temperatures.

Materials	Temperature (°C)	Sensitivity %	Res. time (sec)	Rec. time (sec)
Pure SnO_2	30	6.086	10.8	9.9
	100	13.099	9	10.8
	200	35.751	9	12.6
SnO_2:Mn	30	7.317	7.2	11.7
	100	25.490	10.8	7.2
	200	20.930	6.3	10.8
SnO_2:Cu	30	16.167	7.2	9.9
	100	24.0501	6.3	12.6
	200	17.964	9	10.8
SnO_2:Sb	30	14.876	7.2	11.7
	100	41.666	8.1	9.9
	200	37.113	6.3	10.8

A comparative analysis of the NO_2 sensing performance of this sensor with other sensors documented in the literature is shown in Table 5.

Table 5: Comparison between the NO_2 sensing performance of the SnO_2:Sb gas sensor with other literature results.

Sensing Materials	Working Temperature	Concentration (ppm)	Response	Response–Recovery Time	Reference
SnO_2	RT	0.5	50	84/320	30
Pd-ZnO nanowires	100	1	13.50	141/177 s	31
ZnSe/ZnO	200	8	10.42	98/141s	32
ZnO/In_2O_3	RT	10	29.10	78/610 s	33
SnO2/RGO	200	4	4.56	-	34
In_2O_3: CdO	300	-	78.4	39/49 s	35
SnO_2:Sb	100	50	41.66	8.1/9.9	This work

5. Conclusions

The undoped and doped SnO_2 thin films with different metal dopants (Cu, Mn and Sb) were prepared using the pulsed laser deposition method. The structural, optical, and electrical characteristics are influenced by the different dopants, which affect the gas sensor performance

against NO_2 gas. The addition of dopants created defects, such as oxygen vacancies and lattice distortions, which enhanced the surface area and increased the active sites. The optical bandgap of SnO_2 thin films was modified through doping, which altered the optical absorption and transmittance characteristics. The creation of dopant-induced defects and active sites significantly improved the gas sensor performance by increasing the interaction between the film surface and gas molecules. The Sb dopants demonstrated higher sensitivity toward NO_2 than the other dopants (Cu and Mn), emphasizing the importance of selecting a suitable dopant.

Conflict of Interest

The authors declare no conflicts of interest.

References

1. P. Sivakumar, H. S. Akkera, T. R. Kumar Reddy, Y. Bitla, V. Ganesh, P. M. Kumar, G. S. Reddy and M. Poloju, Effect of Ti doping on structural, optical and electrical properties of SnO_2 transparent conducting thin films deposited by sol-gel spin coating. *Opt. Mater.* **113**, 110845 (2021) https://doi.org/10.1016/j.optmat.2021.110845.
2. N. Y. Elamin, T. Indumathi, and E. R. Kumar, Evaluation of physicochemical and biological properties of SnO_2 and Fe doped SnO_2 nanoparticles. *Ceram. Int.* **49**(2), 2388 (2023). https://doi.org/10.1016/j.ceramint.2022.09.211.
3. I. S. Naji, Characterization of CuO-doped tin dioxide thin films prepared by pulsed-laser deposition for gas-sensing applications. *In: Proceedings of the Institution of Mechanical Engineers, Part N: Journal of Nanomaterials, Nanoengineering and Nanosystems*. **233**(1), 17 (2019). https://doi.org/10.1177/2397791418819267.
4. F. Medjaldi, A. Bouabellou, Y. Bouachiba, A. Taabouche, K. Bouatia and H. Serrar, Study of TiO_2, SnO_2 and nanocomposites TiO_2:SnO_2 thin films prepared by sol-gel method: Successful elaboration of variable–refractive index systems. *Mater. Res. Express*. **7**(1), 016439 (2020). https://doi.org/10.1088/2053-1591/ab6c0c.
5. N. A. AbdulWahhab, Optical properties of SnO_2 thin films prepared by pulsed laser deposition technique. *J. Opt.* **49**, 41 (2020). https://doi.org/10.1007/s12596-020-00587-6.
6. Q. -H. Wu, J. Li, and S. -G. Sun, Nano SnO_2 Gas Sensors. *Curr. Nanosci.* **6**(5), 525 (2010). https://doi.org/10.2174/157341310797574934.
7. I. M. Ibrahim, I. M. Ali, R. M. Al-Haddad, and H. D. Muhammed, Influence of substrate temperature on structural and optical properties of SnO_2 films, *Iraqi J. Phys.* **10**(18), 50 (2012).
8. S. Hooshmand, P. Kassanos, M. Keshavarz, P. Duru, C. I. Kayalan, İ. Kale, and M. K. Bayazit, Wearable nano-based gas sensors for environmental monitoring and encountered challenges in optimization. *Sensors*. **23**(20), 8648 (2023). https://doi.org/10.3390/s23208648.
9. l. Almaev, N. Yakovlev, V. Kopyev, V. Nikolaev, P. Butenko, J. Deng, A. Pechnikov, P. Korusenko, A. Koroleva and E. Zhizhin, High sensitivity low-temperature hydrogen sensors based on SnO_2/κ(ε)-Ga_2O_3:Sn heterostructure. *Chemosensors* **11**(6), 325 (2023). https://doi.org/10.3390/chemosensors11060325.
10. H. Kumari, Sonia, S. Chahal, Suman, P. Kumar, A. Kumar, and R. Parmar, Sol–gel synthesis and characterization of Gd-doped SnO_2 nanoparticles for water treatment and spintronic applications. *J. Mater. Sci.: Mater. Electron*. **35**(3), 212 (2024). https://doi.org/10.1007/s10854-023-11863-z.
11. S. Sambasivama, P. S. Maramb, C. V. V. Muralee Gopic, and I. M. Obaidat, Effect of erbium on the structural, morphological, and optical properties of SnO_2 thin films deposited by spray pyrolysis. Optik, **202**, 163596 (2020). https://doi.org/10.1016/j.ijleo.2019.163596.
12. Y. Tao, B. Zhu, Y. Yang, J. Wu, and X. Shi, The structural, electrical, and optical properties of SnO_2 films prepared by reactive magnetron sputtering: Influence of substrate temperature and O_2 flow rate. *Mater. Chem. Phys.* **250**, 123129, (2020). https://doi.org/10.1016/j.matchemphys.2020.123129.
13. K. H. Kim and J. S. Chun, X-ray studies of SnO_2 prepared by chemical vapour deposition. Thin Solid Films, **141**(2), 287 (1986). https://doi.org/10.1016/0040-6090(86)90356-1.
14. H. Meddas, L. Abdelghani, D. Amel, B. Saliha, S. Randa, and B. Okba, Spin coating deposition of tin oxide thin films: Influence of solution concentration. *J. Chem. Res.* **48**(5), 10 (2024). https://doi.org/10.1177/17475198241277728.
15. M. Sharma, R. N. Aljawfi, K. Kumari, K. H. Chae, S. Dalela, S. Gautam, P. A. Alvi, and S. Kumar, Investigation of local geometrical structure, electronic state and magnetic properties of PLD grown Ni doped SnO_2 thin films. *J. Electron Spectros. Relat. Phenomena*. **232**, 21 (2019). https://doi.org/10.1016/j.elspec.2019.01.002.

16. J. M. Conde Garrido, and J. M. Silveyra, A review of typical PLD arrangements: Challenges, awareness, and solutions. Opt. Lasers Eng. **168**, 107677 (2023). https://doi.org/10.1016/j.optlaseng.2023.107677.
17. S. H. Rashed, A. J. Haider, S. Younis, Characterization of the copper oxide thin films deposited by DC sputtering technique. *Eng. Tech. J.* **32** Part (B) (4), 770 (2014).
18. J. M. Rzaij, S. O. Nawaf, and A. K. Ibrahim, A review on tin dioxide gas sensor: The role of the metal oxide doping, nanoparticles, and operating temperatures. *World J. Adv. Res. Rev.* **14**(1), 051 (2022). https://doi.org/10.30574/wjarr.2022.14.1.0288.
19. B. A. Hasan, D.C conductivity of In_2O_3: SnO_2 thin films and manufacturing of gas sensor. *Iraqi J. Phys.* **16**(37), 32 (2018). https://doi.org/10.30723/ijp.v16i37.74.
20. Y. Xiong, Y. Lin, X. Wang, Y. Zhao, and J. Tian, Defect engineering on SnO_2 nanomaterials for enhanced gas sensing performances. *Adv. Powder Mater.* **1**(3), 100033 (2022). https://doi.org/10.1016/j.apmate.2022.02.001.
21. L. K. Dintle, P. V. C. Luhanga, C. Moditswe, and C. M. Muiva, Compositional dependence of optical and electrical properties of indium doped zinc oxide (IZO) thin films deposited by chemical spray pyrolysis. *Phys. E Low-Dimensional Syst. Nanostructures*. **99**, 91 (2018). https://doi.org/10.1016/j.physe.2018.01.009.
22. R. Vinodkumar, K. J. Lethy, and D. Beena, Effect of thermal annealing on the structural and optical properties of nanostructured zinc oxide thin films prepared by pulsed laser ablation. *Sol. Energy Mater. Sol Cells.* **93**(1), 74 (2009). https://doi.org/10.1016/j.solmat.2008.04.014.
23. S. Roguai and A. Djelloul, Structural, morphological, optical and electrical properties of Ni-doped SnO_2 thin films by pneumatic spray pyrolysis method. *Bull. Mater. Sci.* **45**, 227 (2022). https://doi.org/10.1007/s12034-022-02804-3.
24. M. Karmaoui, A. B. Jorge, P. F. McMillan, A. E. Aliev, R. C. Pullar, J. A. Labrincha, and D. M. Tobaldi**,** One-step synthesis, structure, and band gap properties of SnO_2 nanoparticles made by a low temperature nonaqueous sol–gel technique. *ACS Omega.* **3**(10), 13227 (2018). https://doi.org/10.1021/acsomega.8b02102.
25. S. D. Ponja, B. A. D. Williamson, S. Sathasivam, D. O. Scanlon, I. P. Parkin, and C. J. Carmalt, Enhanced electrical properties of antimony doped tin oxide thin films deposited *via* aerosol assisted chemical vapour deposition. *J. Mater. Chem. C.* **6**(27), 7257 (2018). https://doi.org/10.1039/c8tc01929k.
26. S. S. Soumya, R. Vinodkumar, and N. V. Unnikrishnan, Conductivity type inversion and optical properties of aluminium doped SnO_2 thin films prepared by sol-gel spin coating technique. *J Sol-Gel Sci Technol*. **99**, 636 (2021). https://doi.org/10.1007/s10971-021-05599-7.
27. V. S. Bhati, M. Hojamberdiev, and M. Kumar, Enhanced sensing performance of ZnO nanostructures-based gas sensors: A review. *Energy Rep.* **6**(4), 46 (2020). https://doi.org/10.1016/j.egyr.2019.08.070.
28. Y. F. Sun, S. B. Liu, F. L. Meng, J. Y. .Liu, Z. Jin, L. T. Kong, and J. H. Liu, Metal Oxide Nanostructures and Their Gas Sensing Properties: A Review. Sensors **12**(3), 2610 (2012). https://doi.org/10.3390/s120302610.
29. L. Francioso, A. Forleo, S. Capone, M. Epifani, A. M. Taurino, and P. Siciliano, Nanostructured In_2O_3–SnO_2 sol–gel thin film as material for NO_2 detection. *Sens. Actuators B Chem.* **114**(2), 646 (2006). https://doi.org/10.1016/j.snb.2005.03.124.
30. R. Kumar, Mamta, R. Kumari and V. N. Singh, SnO_2-Based NO_2 Gas Sensor with Outstanding Sensing Performance at Room Temperature. *Micromachines*. **14**(4), 728 (2023). https://doi.org/10.3390/mi14040728.
31. X. Chen, Y. Shen, P. Zhou, S. Zhao, X. Zhong, T. Li, C. Han, D. Wei, D. Meng, NO_2 sensing properties of one-pot-synthesized ZnO nanowires with Pd functionalization. *Sens. Actuators B Chem.* **280**, 151 (2019). https://doi.org/10.1016/j.snb.2018.10.063.
32. W. Liu, D. Gu, X. Li, Ultrasensitive NO_2 Detection Utilizing Mesoporous ZnSe/ZnO Heterojunction-Based Chemiresistive-Type Sensors. *ACS Appl. Mater. Interfaces*, **11**(32), 29029 (2019). https://doi.org/10.1021/acsami.9b07263.
33. X. Liang, J. Zhang, L. Du, and M. Zhang, Effect of resonant tunneling modulation on ZnO/In_2O_3 heterojunction nanocomposite in efficient detection of NO_2 gas at room temperature. *Sens. Actuators B Chem.* **329**(32), 129230 (2021). https://doi.org/10.1016/j.snb.2020.129230.
34. B. Bhangare, N. S. Ramgir, S. Jagtap, A. K. Debnath, K. P. Muthe, C. Terashima, D. K. Aswal, S. W. Gosavi, and A. Fujishima, XPS and Kelvin probe studies of SnO_2/RGO nanohybrids based NO_2 sensors. *Appl Surf Sci.* **487**, 918 (2019). https://doi.org/10.1016/j.apsusc.2019.05.176.
35. A. T. Dahham, K. A. Aadim, and N. K. Abbas, Synthesis and Fabrication of In2O3: CdO Nanoparticles for NO_2 Gas Sensor. *Baghdad Sci. J.* **15**(3), 292 (2018). http://dx.doi.org/10.21123/bsj.2018.15.3.0292.

تأثير الشوائب على الخصائص التركيبية والبصرية لأغشية اوكسيد القصدير الرقيقة المترسبة بتقنية الترسيب الليزري النبضي لتطبيقات أجهزة استشعار الغاز

اسماعيل سعدون نجم[1] واقبال سهام ناجي[1]
[1]قسم الفيزياء، كلية العلوم، جامعة بغداد، بغداد، العراق

الخلاصة

كشفت هذه الدراسة عن تأثير الشوائب المختلفة (المنغنيز، والنحاس، والأنتيمون) على خصائص أغشية أكسيد القصدير الرقيقة المُحضّرة بتقنية الترسيب بالليزر النبضي. تم تحضير المساحيق النقية والمطعمة بتقنية سول-جل، ثم تم تلبيدها عند 600 درجة مئوية لمدة ساعتين. أظهر التحليل البنيوي بنية رباعية لأكسيد القصدير، وأن إضافة الشوائب أدت إلى زيادة إجهاد الشبكة البلورية وكثافة الانخلاعات، مما عزز المواقع النشطة المتاحة لتفاعلات الغاز. وكشف تحليل الشكل المورفولوجي أن الجسيمات موزعة بانتظام في الأغشية، وأنها كروية الشكل تقريبًا. وأظهرت القياسات البصرية تغيرًا في فجوة الطاقة، حيث انخفضت مع التطعيم من 3.83 إلكترون فولت إلى 2.86 إلكترون فولت. وبلغت الحساسية الأعلى تجاه 50 جزءًا في المليون من ثاني أكسيد النيتروجين عند درجة حرارة تشغيل 100 درجة مئوية 41.6% للغشاء المُطعم بالأنتيمون، مقارنةً بالأغشية المُطعمة بالمنغنيز والنحاس (25% و24% على التوالي). أظهرت النتائج التأثيرات المختلفة للمواد المضافة المختلفة في تعزيز الخصائص الهيكلية والبصرية للأغشية الرقيقة من اوكسيد القصدير، والتي تؤثر على حساسية المستشعر تجاه غاز ثاني أكسيد النيتروجين.

الكلمات المفتاحية: اوكسيد القصدير، الاغشية الرقيقة، طريقة الترسيب الليزري النبضي، تطعيم اوكسيد القصدير، متحسس الغاز.